Observations of the Madden Julian Oscillation during Indian Ocean Dipole events

Earle A. Wilson,[1] Arnold L. Gordon,[1,2] and Daehyun Kim[1]

Received 5 June 2012; revised 29 January 2013; accepted 31 January 2013.

[1] The characteristics of Madden Julian Oscillation (MJO) development and propagation during Indian Ocean Dipole (IOD) events are presented in this study. We find that MJO activity over the Indian Ocean and Maritime Continent is enhanced during negative IOD and subdued during positive IOD. MJO events occurring during positive IOD have weaker convection and less organized wind anomalies than those occurring during neutral or negative IOD. These differences are starkest over the eastern Indian Ocean where the IOD has the greatest effect on low-level humidity. Based on these observations and current MJO theories, we posit that the IOD primarily influences the MJO through its modulation of local low-level moisture.

Citation: Wilson, E. A., A. L. Gordon, and D. Kim (2013), Observations of the Madden Julian Oscillation during Indian Ocean Dipole events, *J. Geophys. Res. Atmos.*, *118*, doi:10.1002/jgrd.50241.

1. Introduction

[2] The Madden Julian Oscillation (MJO) is the dominant mode of intraseasonal (30–90 day) variability in the tropical atmosphere [*Madden and Julian*, 1971]. It is a planetary-scale disturbance consisting of convective anomalies, coupled to anomalous circulation, that together propagate eastward at an average speed of approximately 5 m/s [*Madden and Julian*, 1972]. Despite being the subject of intensive research over the past few decades, the MJO's physical mechanisms remain unsatisfactorily explained [*Zhang*, 2005]. Several models have been proposed, but none has been able to quantitatively capture the frequency, zonal scales, and eastward propagating speed of the MJO [*Zhang*, 2005]. One particular source of dispute is the extent to which sea surface temperature variability affects the MJO. This uncertainty has led many studies to investigate the MJO's relationship with ENSO [e.g., Kressler *et al*., 1995; *Zhang and Gottschalk*, 2002; *Hendon et al*., 2007]; however, only a few have examined its relationship with the Indian Ocean Dipole (IOD).

[3] Like its Pacific counterpart, the tropical Indian Ocean has its own mode of interannual variability. The sea surface temperature (SST) anomaly pattern associated with this interannual mode has a distinct zonal dipole structure, hence the IOD [*Saji et al.*, 1999]. The IOD exhibits strong seasonality; its events tend to develop during boreal summer, peak in the fall, and collapse at the onset of winter. Positive IOD is characterized by cool SST anomalies over the eastern Indian Ocean near Sumatra and warm SST anomalies over much of the western Indian Ocean—in other words, a flattening of the seasonal zonal SST gradient [*Saji et al*., 1999; *Webster et al*., 1999]. Accompanying this change are low-level easterly anomalies along the equator, which represents a weakening of the seasonal equatorial low-level westerlies. Negative IOD is characterized by an opposite set of anomalies.

[4] Several studies have provided us with clues as to how the IOD might affect the MJO. *Shinoda and Han* [2005] found that subseasonal (6–90 day) surface zonal wind variability is suppressed (enhanced) during positive (negative) IOD events. Similarly, *Sooraj et al.* [2009], using simulations from atmospheric and coupled global circulation models, showed that there is significant correlation between high-frequency (2–90 day) and low-frequency wind variability over the Indian Ocean. They attributed this relationship to variations in vertical wind shear, whereby easterly vertical wind shear in the low frequency wind enhances variability in high frequency wind. *Kug et al.* [2009] came to an equivalent conclusion after analyzing the variance of observed (2–70 day) 850 mbar zonal wind anomalies during different IOD events. This led them to infer that the MJO would be enhanced (subdued) during negative (positive) IOD.

[5] The Indian Ocean region is uniquely important to the MJO. Primary MJO events—events not preceded by others—preferentially initiate over the Indian Ocean; the region accounts for 40% of all starting locations [*Matthews*, 2008]. Furthermore, the MJO's convective signal tends to peak over the warm pool region, which extends from the tropical Indian Ocean to the western Pacific [*Madden and Julian*, 1972; *Knutson and Weickmann*, 1987]. Therefore, any change in MJO behavior over the Indian Ocean could lead to major changes in intraseasonal variability globally.

[6] This study seeks to explore the relationship between the MJO and the IOD in further detail. We will examine

[1]Lamont-Doherty Earth Observatory, Columbia University, Palisades, NY, USA.
[2]Department of Earth and Environmental Sciences, Columbia University, New York, NY, USA.

Corresponding author: E. A. Wilson, Box 357940, Seattle, WA, 98195 USA. (ewilson@ldeo.columbia.edu)

2169-897X/13/10.1002/jgrd.50241

the MJO's development during different IOD events and, in doing so, attempt to explain the mechanisms that permit any observed interaction. Since the IOD and the MJO exist on intraseasonal and interannual timescales, respectively, our results will also reveal the sensitivity of the MJO to climatological variability over the Indian Ocean.

2. Methodology

2.1. Data

[7] This study uses data from a variety of observational, reconstructed, and reanalysis data sets. Sea level pressure (SLP), u-wind, v-wind, and specific humidity data are obtained from the National Centers for Environmental Prediction (NCEP) reanalysis data set [*Kalnay et al.* 1996]. Outgoing Longwave Radiation (OLR) and sea surface temperature (SST) data are sourced from the NCEP/NOAA interpolated OLR data set [*Liebmann and Smith*, 1996] and NOAA Extended Reconstructed SST V3b data set [*Smith et al.*, 2008], respectively. All data are analyzed on a $2.5^\circ \times 2.5^\circ$ spatial grid for the time period 1 January 1979 to 31 December 2010.

[8] Daily anomalies are obtained by first removing the linear trend and daily climatology from the time series of each spatial grid point. The linear trend is derived from a least squares fit, and the daily climatology is the average of each calendar day (excluding 29 February) over the 32 year period. The daily anomalies are then treated with a 30–90 day band pass Lanczos filter using 401 weights [*Duchon*, 1979]. In doing so, the first and last 200 days of the time series are discarded. These filtered daily anomalies are used to diagnose variability on the intraseasonal time scale. To obtain monthly anomalies, the linear trend and climatological monthly means are simply subtracted from the monthly time series of each spatial grid point. These monthly anomalies are used to investigate variability on the interannual time scale, such as those driven by IOD or ENSO.

[9] Owing to the seasonality of the IOD, this study focuses on events that occur between August and November (ASON months), when the IOD is typically in its mature state. The seasonality of the IOD is slightly out of sync with that of the MJO, which tends to be most vigorous during northern winter and slightly weaker in the fall [*Salby and Hendon*, 1994; *Wheeler and Kiladis*, 1999]. Therefore, the results presented here are biased towards the weaker fall MJO events.

2.2. Finding MJO and IOD events

2.2.1. The RMM Index

[10] To isolate individual MJO events, we use the Wheeler and Hendon Real-time Multivariate MJO (RMM) index [*Wheeler and Hendon*, 2004]. This index is composed of the principal component time series, RMM1 and RMM2, of the leading pair of empirically orthogonal functions of combined near-equatorially averaged OLR, 200 mbar zonal winds, and 850 mbar zonal winds. In other words, the index measures MJO activity by analyzing the combined spatial variations of OLR and upper/lower level zonal winds across the equator. Since the MJO is characterized by a coupling between deep convection and circulation, the RMM index is well suited to capture the MJO's multivariate structure. Daily RMM values are obtained from an online database maintained by Matthew Wheeler (http://www.cawcr.gov.au/staff/mwheeler/maproom/RMM/RMM1RMM2.74toRealtime.txt).

[11] It is often convenient to map the RMM index into "RMM space," where RMM1 and RMM2 define a pair of orthogonal axes. In this phase space, one can plot daily RMM1 and RMM2 values as individual points (see Figure 6 for quick reference). For an eastward propagating MJO event, the RMM index conveniently traces a counterclockwise arc in this basis. Exploiting this feature, RMM space is often divided into eight sections or RMM phases that roughly capture the longitudinal location of the active phase of the MJO. The amplitude of the RMM index, given by square root of $\mathrm{RMM1}^2 + \mathrm{RMM2}^2$, is a measure of MJO strength. Following convention, significant/strong MJO activity is taken to be when the RMM amplitude is greater than 1.

[12] Since introduced by *Wheeler and Hendon* [2004], the RMM index quickly became one of the leading measures of MJO activity. However, as with any other index, we should be mindful of the RMM index's constraints. Some of these limitations have come to light in recent studies such as *Roundy et al.* [2009] and *Straub* [2012].

[13] *Roundy et al.* [2009] showed that signals from other convectively coupled waves, namely, equatorial Kelvin and Rossby waves, can have a non-negligible impact on the RMM index. They demonstrated that a large-amplitude Kelvin wave can contribute up to a 0.3 standard deviation shift in the RMM index. Notwithstanding this limitation, the RMM index is still dominated by signals associated with the MJO; a large amplitude (standard deviation > 1), counterclockwise signal in RMM space all but guarantees the presence of an MJO event.

[14] *Straub* [2012] demonstrated that the RMM index is more sensitive to patterns in the circulation field than those in the OLR field. This puts the RMM index at a disadvantage when the primary goal is to observe the MJO's convective development. Since we are interested in both the MJO's convection and circulation, the RMM index's slight bias towards the circulation field is not a major concern. Nevertheless, it will be important to analyze the convection and circulation anomalies directly—as we do later in this study. *Straub* [2012] also points out that since the RMM index is defined on a global scale, it may not be able to detect local developments. This puts the RMM index at a major disadvantage when the goal is to study MJO initiation. This constraint is also not a major concern for this study since MJO initiation is not our focus.

2.2.2. The Dipole Mode Index

[15] IOD activity is conventionally described by the Dipole Mode Index (DMI) [*Saji et al.*, 1999]. The DMI is defined as the difference between SST anomalies over the western Indian Ocean, 50°E–70°E and 10°S–10°N, and the eastern Indian Ocean, 90°E–110°E and 0°S–10°S. In this study, the DMI is computed using the aforementioned monthly SST anomalies. The final index is smoothed with a 3 month running mean and normalized by the standard deviation of the entire time series. IOD events are defined as periods when the DMI varies by more than 1 standard deviation.

[16] The extent to which the IOD depends on ENSO is a controversial issue. Studies such as *Webster et al.* [1999]

and *Saji et al.* [1999] argue on behalf of their independence, which is, in part, supported by the relatively weak correlation (< 0.35) between the DMI and the Niño 3.4 SST index supports. However, this correlation increases to 0.56 during ASON months. While a correlation of ~0.6 implies dependent evolution, it also means that the Niño 3.4 index can only explain roughly one third of the variance in the DMI during ASON months. Figure 1 shows the time series for the two indices; instances of concurrent evolution are evident, but this is not always the case. This study does not seek to resolve the dependency of the IOD on ENSO (or vice versa). Rather, the main concern is to ensure that the IOD can influence intraseasonal atmospheric variability over the Indian Ocean region, with or without the influence of ENSO. Doing so will give us confidence that the changes in atmospheric variability that occur during IOD events are not simply a remote response to ENSO.

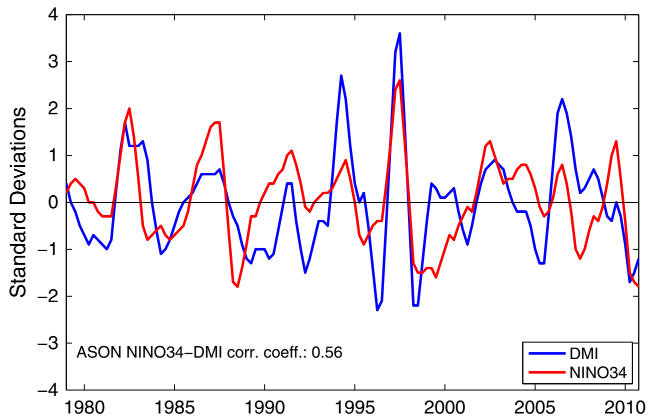

Figure 1. Time series of the Dipole Mode Index (DMI) and the Niño 3.4 SST index for ASON months only. Both indices are normalized by the standard deviations of their full time series.

3. Results

3.1. The IOD's Forcing

[17] Figure 2 shows composites of SST and specific humidity anomalies during positive and negative IOD. Specific humidity is averaged from 850 to 500 millibars (mbar), which accounts for the lower troposphere just above the planetary boundary layer. The SST anomalies over the Indian Ocean exhibit a distinct dipole pattern. The eastern half of the dipole is concentrated just south of Sumatra but extends through Indonesia and into the western Pacific. The humidity anomalies are mostly manifested over the southeastern tropical Indian Ocean and Maritime Continent. Over these regions, dry (moist) anomalies persist during positive (negative) IOD. During positive IOD, positive humidity

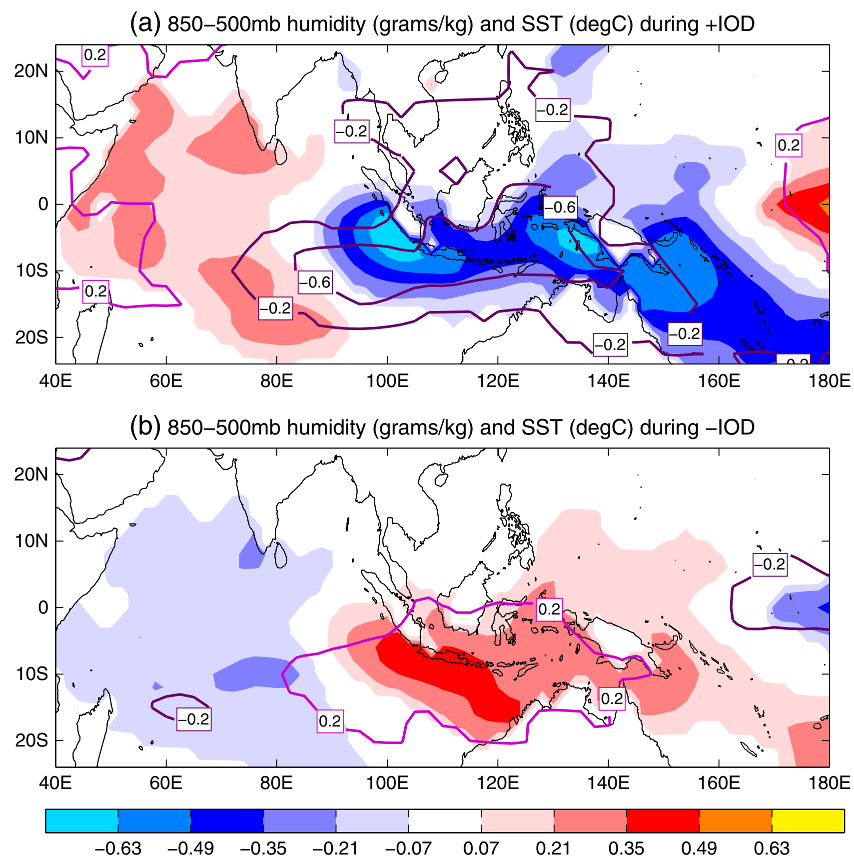

Figure 2. (a) SST (°C/shading) and 850–500 mbar specific humidity (g kg^{-1}/contours) anomalies during positive IOD. (b) Same as in Figure 2a but during negative IOD. Light and dark contours represent positive and negative values, respectively. Only anomalies exceeding 95% significance, based on a two-tailed Student's *t* test, are shown.

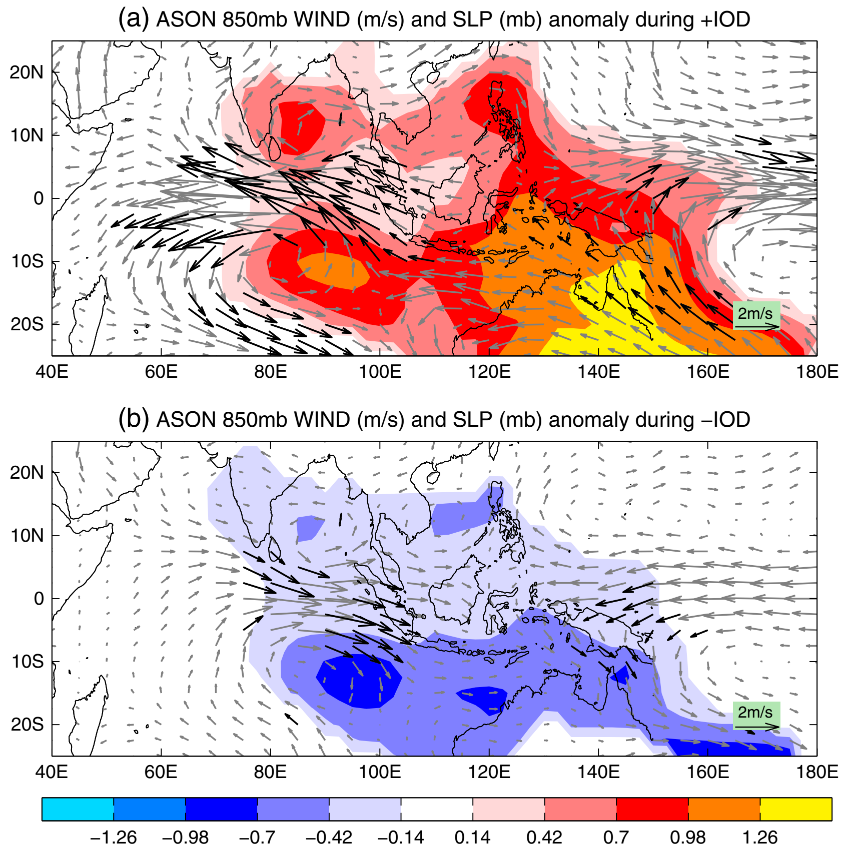

Figure 3. (a) SLP (mbar) and 850 mbar wind (ms^{-1}) anomalies during positive IOD. (b) Same as in Figure 3a but during negative IOD. Anomalies exceeding 95% significance are indicated by shading and bold arrows.

anomalies are observed over the western Indian Ocean. These humidity patterns coincide with the rainfall anomaly patterns shown in *Saji et al.* [1999] and the OLR anomaly patterns shown in *Shinoda and Han* [2005].

[18] Figure 3 features composites of SLP and 850 mbar winds during both IOD modes. During positive IOD, SLP increases throughout most of the region, from 80°E to 160°E, which coincides with the anomalous low-level wind flow out of the Maritime Continent (Figure 3a). Negative IOD shows an opposite, albeit slightly weaker, anomalous flow. In this case, low-level winds flow into the eastern Indian Ocean and Maritime Continent region at a greater rate than usual. Over the southeastern Indian Ocean, there is an anomalous high-pressure anticyclone; to the north, at about 10°N, there is a slightly weaker anticyclone. At 850 mbar, these anticyclones are shifted slightly west of the SLP anomalies.

3.2. IOD Influence on Intraseasonal Variability

[19] Next, we observe how the IOD affects intraseasonal activity over the Indian Ocean region. To facilitate this analysis, we use the variance of 30–90 day filtered OLR and 850 mbar zonal wind anomalies as proxies for intraseasonal activity. The variance of the filtered anomalies is calculated within a 3 month moving window; that is, the variance value at any given day is calculated over the subsequent 3 months. As a result, the final 3 months of each time series are truncated in this analysis.

[20] Figure 4a shows the correlation coefficients of filtered OLR variance against the DMI for ASON months. Over the eastern Indian Ocean, intraseasonal variability in OLR is inversely related to the DMI. That is, OLR intraseasonal variability is suppressed over the eastern Indian Ocean during positive IOD and enhanced during negative IOD. This agrees with the findings of *Kug et al.* [2009] and *Shinoda and Han* [2005]. Additionally, these correlation patterns over the eastern Indian Ocean are split near the equator. These two lobes of significant correlation spatially overlap with the anomalous (anti)cyclonic cells shown from Figure 3. Further west near Africa, intraseasonal OLR variability has a positive relationship with the DMI. *Saji et al.* [1999] noted that positive IOD enhances rainfall over the western Indian Ocean and eastern Africa while suppressing rainfall over eastern Indian Ocean and Indonesia.

[21] Given the significant correlation between ENSO and IOD activity, much of what is shown in Figure 4a could be a direct effect of ENSO. To properly account for the IOD's effect on intraseasonal variability, ENSO's contribution needs to be estimated and removed. Following *Saji and Yamagata* [2003] and *Kug et al.* [2009], we use partial correlation to remove ENSO's contribution to intraseasonal

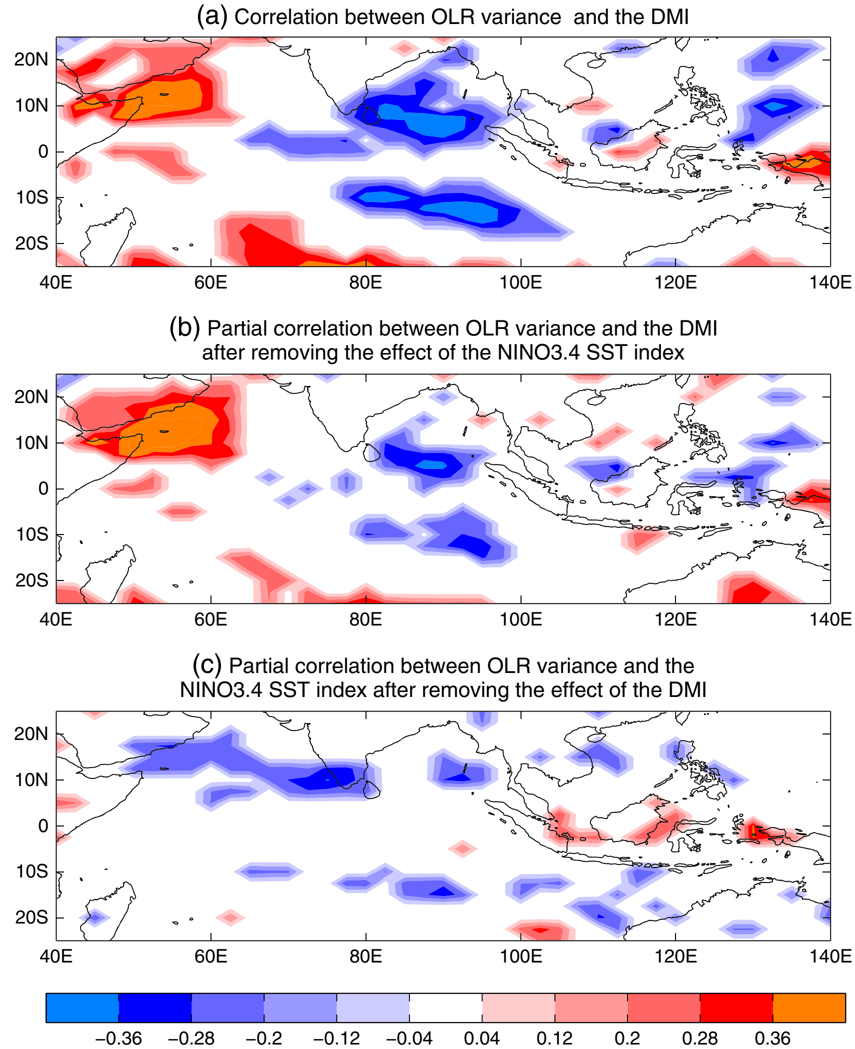

Figure 4. (a) Correlation between 30–90 day OLR variance and the DMI. (b) Partial correlation between 30–90 day OLR variance and DMI while controlling for the effect of ENSO via the NINO3.4 SST index. (c) Partial correlation between OLR wind variance and the NINO3.4 SST index while controlling for the effect of the DMI. Calculations are done for ASON months only. Correlation coefficients are significant at a 95% confidence level.

variance. The partial correlation equation is given by the following:

$$P_c^{AB} = \frac{(R_{AB} - R_{AC}\,R_{BC})}{\sqrt{\left(1 - R_{AC}^2\right)\left(1 - R_{BC}^2\right)}} \qquad (1)$$

where P_c^{AB} is the partial correlation between two random variables, A and B, after removing the controlling effect of another random variable, C [*Panofsky and Brier*, 1958]. Variables A, B, and C can be taken as OLR variance, the DMI, and the Niño 3.4 SST index, respectively. In this case, R_{AB} and R_{AC} are the simple correlations between OLR variance and the DMI, and OLR variance and the Niño 3.4 SST index, respectively. Likewise, R_{BC} is the simple correlation between the DMI and Niño 3.4 indices. In essence, P_c^{AB} is a measure of the variance in OLR that is estimated by the DMI but not by the Niño 3.4 index. Additionally, if we reverse the roles of B and C, P_c^{AB} would become a measure of the variance in OLR estimated by the Niño 3.4 index but not by the DMI.

[22] Figure 4b shows the partial correlation between intraseasonal OLR variability and the DMI after removing the variance explained by the Niño 3.4 SST index. The resulting correlations are slightly reduced, but much of the structure from Figure 4a is retained. In other words, Figure 4b shows that there is still a significant relationship between the IOD and intraseasonal OLR variability even after removing the variance accounted for by the Niño 3.4 SST index. However, the same is not true when the roles of the DMI and Niño 3.4 SST index are interchanged. Figure 4c shows the partial correlation between intraseasonal OLR variability and the Niño 3.4 SST index after removing the variance explained by the DMI. In this case, there is hardly any correlation between the Niño 3.4 SST index and intraseasonal OLR variability. With these results, we can conclude with more assurance that the correlation map in Figure 4a is not simply a remote effect of ENSO and that the IOD likely has some direct control on OLR variability over the Indian Ocean.

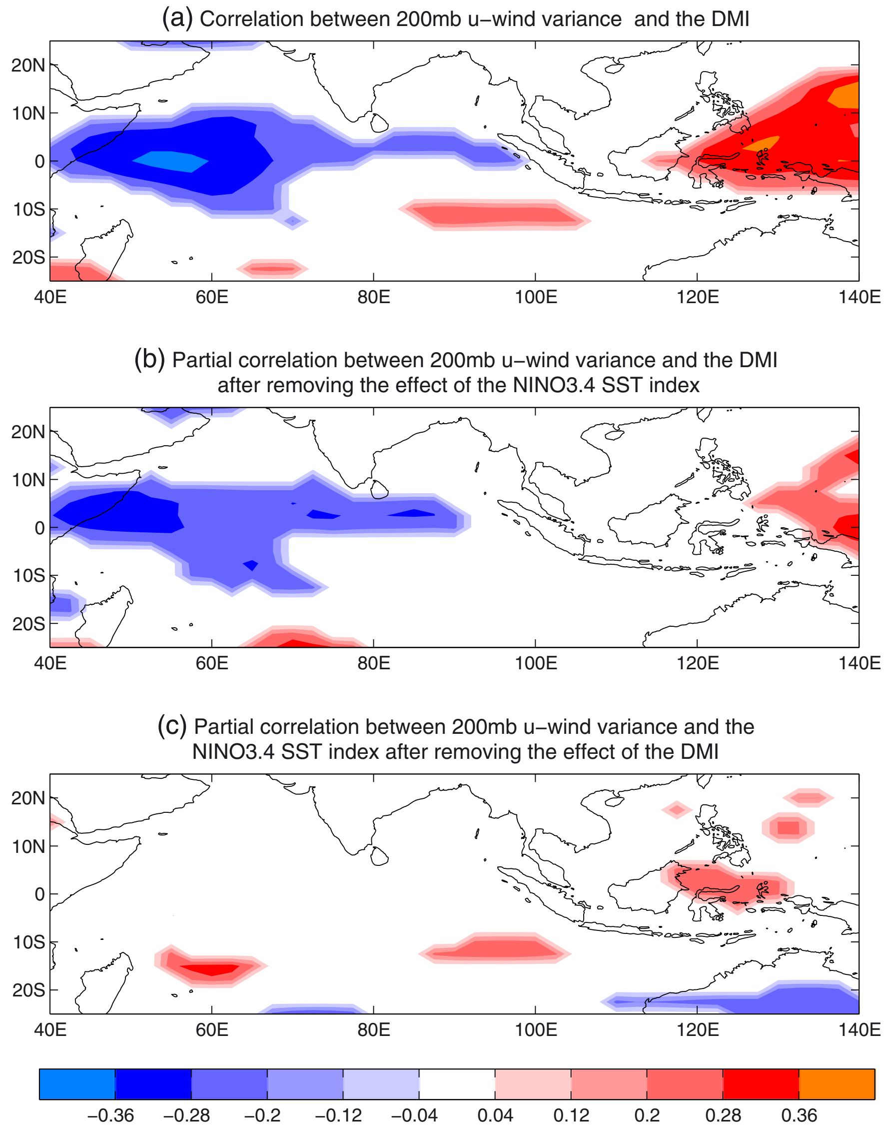

Figure 5. Same as Figure 5 but for 30–90 day 200 mbar zonal wind variance.

[23] Figure 5 shows a similar set of plots but for the variance of 200 mbar zonal winds correlated with the DMI. As with Figure 4, there is an inverse relationship between intraseasonal zonal wind variability and the DMI across the Indian Ocean basin. In Figure 5a, the correlation pattern is monolithic and spans across much of the equatorial western Indian Ocean. To the far east, there are significant positive correlation values extending from the Pacific. These positive correlations are likely due to ENSO rather than the IOD. Indeed, when the effect of the Niño 3.4 SST index is removed, the correlation values in the east are substantially reduced (Figure 5b), while those to the west are relatively unchanged. When the roles of the Niño 3.4 SST index and the DMI are reversed, the resulting partial correlation map shows almost no relationship between the Niño 3.4 SST index and intraseasonal 200 mbar zonal wind variability (Figure 5c). Once again, we can conclude that the correlation map shown in Figure 5a is better explained by the IOD than ENSO.

[24] The same analysis was repeated for 850 mbar zonal winds. In that instance, intraseasonal wind variability is negatively correlated with the DMI across the eastern Indian Ocean (not shown). However, after removing the variance accounted for by the Niño 3.4 SST index, most of the significant correlation in this region vanishes.

[25] This correlation analysis suggests that the IOD has measurable control over intraseasonal variability throughout the Indian Ocean region; this remains true even after removing the variability accounted for by ENSO. This does not quite hold for 850 mbar wind variability, however, where ENSO accounts for at least as much variance as the IOD. We also observe that the effect of ENSO tends to be additive; the conditions associated with La Niña and El niño events tend to reinforce those associated with negative and positive IOD events, respectively. This can be inferred by comparing Figure 4a with Figure 4b, for the case of OLR, and Figures 5a and 5b, for the case of 200 mbar zonal winds. For these reasons, we posit that the IOD has a significant

impact on intraseasonal variability over the Indian Ocean region but acknowledge that this effect may be amplified by a concurring ENSO event.

3.3. IOD Impact on MJO Activity

[26] MJO events are often described using composites of anomalies, such as OLR and winds, for each RMM phase [e.g., *Wheeler and Hendon*, 2004, Figs. 9 and 10]. Such composites, while very useful, may not truly represent the behavior of individual events. In reality, many MJO events do not cycle through all eight RMM phases. Some MJO events completely dissipate before completing a full cycle. Others degenerate into incoherent activity in one region but reinvigorate in another. Such behavior is more common during northern summer and fall seasons when MJO events are relatively weak.

[27] To better capture the intermittent nature of fall MJO events, we define an MJO event as any period when the amplitude of the RMM index is greater than 1 for at least 5 days. The first step is to smooth the RMM index with a 3 day running mean. This helps to remove some of the high-frequency noise in the index. Next, the smoothed RMM index is screened for a particular RMM phase, say RMM phase 1—this will allow us to analyze MJO behavior within specific regions. MJO events belonging to RMM phase 1 are then found by sliding a 10 day window through the index and finding instances when the amplitude of the RMM index is greater than 1 for at least 5 days within the 10 day window. The 5 days of MJO activity do not all have to be in the same RMM phase. If a MJO event spends 4 days in RMM phase 1 and a fifth day in RMM phase 2, the MJO event will still be counted as passing through RMM phase 1. Further, to avoid counting an MJO event more than once, MJO events occurring within a particular RMM phase are constrained to be at least 30 days apart—the minimum time needed for a full MJO cycle. Following this procedure for the length of the RMM time series gives all the instances when an MJO event passes through RMM phase 1. This is repeated for RMM phase 2 and so forth.

3.3.1. Propagation in RMM Phase Space

[28] Figure 6 shows the composite trajectories of MJO events occurring during negative, positive, and neutral IOD, represented by magenta, blue, and black lines, respectively. Green boxes show where the events begin in

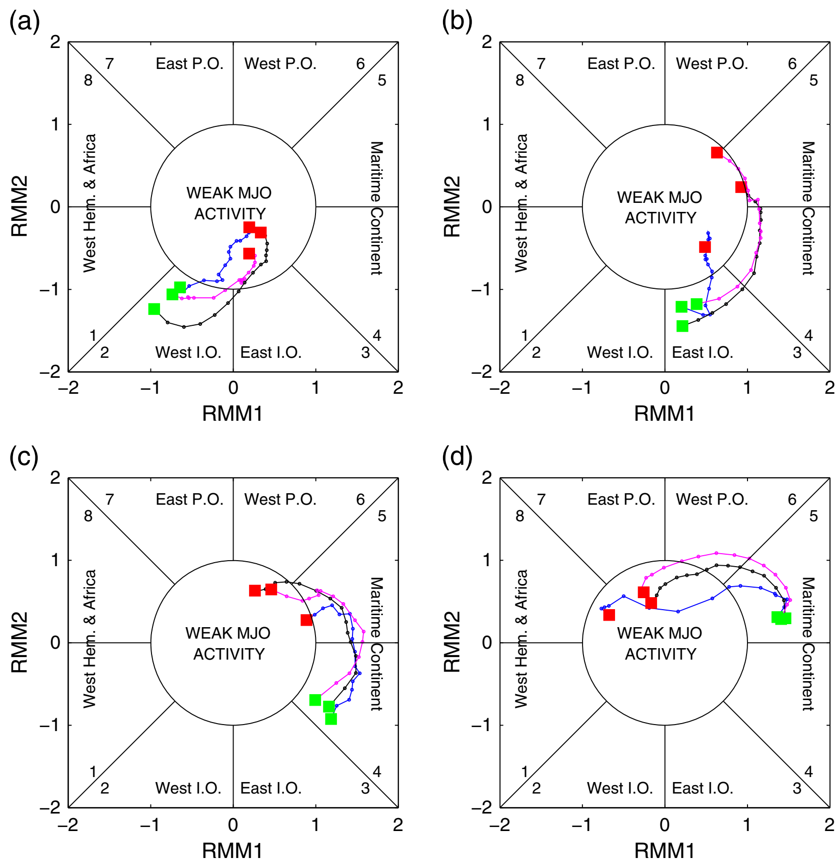

Figure 6. Composite trajectories in RMM phase space for MJO events that occurred during positive, negative, and neutral IOD. RMM refers to the Real-time Multivariate MJO index [*Wheeler and Hendon*, 2004]. (a–d) The evolution of MJO events as they enter RMM phases 2 through 5. The blue, black, and magenta lines represent MJO events that occurred during positive, neutral, and negative IOD, respectively. Green boxes represent where the MJO events begin in each phase, and red boxes show their locations 15 days later. Weak MJO activity is defined by RMM amplitude <1. The number of MJO events during each IOD mode is given in parentheses above each plot.

each phase and red boxes show their location 15 days later. Given the spatial extent of its forcings, the IOD is likely to have the greatest impact when the MJO's convective activity is situated over the Indian Ocean and Indonesia. This is represented by RMM phases 2 through 5 (Figures 6a–6d).

[29] Each of the trajectories in Figure 6 represents instances when equatorial atmospheric conditions exhibited signs of MJO activity–enough to make the amplitude of the RMM index hover above 1 standard deviation for at least 5 days. As is evident, many of these promising MJO events subside before completing a full cycle. The inclusion of these short-lived MJO events is a departure from the more typical procedure of only recognizing events that are strong enough to complete a full cycle. However, by including them, we are better able to observe how the IOD contributes to the MJO's development.

[30] In most cases, MJO propagation was weakest during positive IOD. This is most apparent in Figure 6b, when convection is centered over the eastern Indian Ocean. In this region, most MJO events dissipate almost immediately during positive IOD. MJO events occurring during negative IOD were relatively weak during RMM phase 2 but appeared to strengthen as convective activity shifted to the eastern Indian Ocean and Maritime Continent. All together, Figures 6a–6d suggest that the eastern Indian Ocean and Maritime Continent regions are more (less) favorable for MJO activity during negative (positive) IOD.

3.3.2. OLR and Wind Propagation

[31] Next, we observe how the IOD affects the MJO in the OLR and zonal wind fields directly. Figure 7 shows the time lagged composites of OLR (shading) and 200 mbar wind (contours) anomalies averaged across 10°N and 5°S. This latitude band is chosen because the anomalies, on average, tended to propagate slightly north of the equator during the ASON season. Time 0 is the day when MJO events first enter RMM phase 3, i.e., the green squares in Figure 6b, and the time range now extends from day –20 to day +30. S_{olr} and S_{wnd} are the propagation speeds of the negative OLR anomalies and positive 200 mbar zonal wind (easterly) anomalies. The phase speeds are derived by fitting a weighted regression line through the respective anomaly distributions. The weights are determined by the magnitude of the anomalies at each point. The uncertainty in the speeds

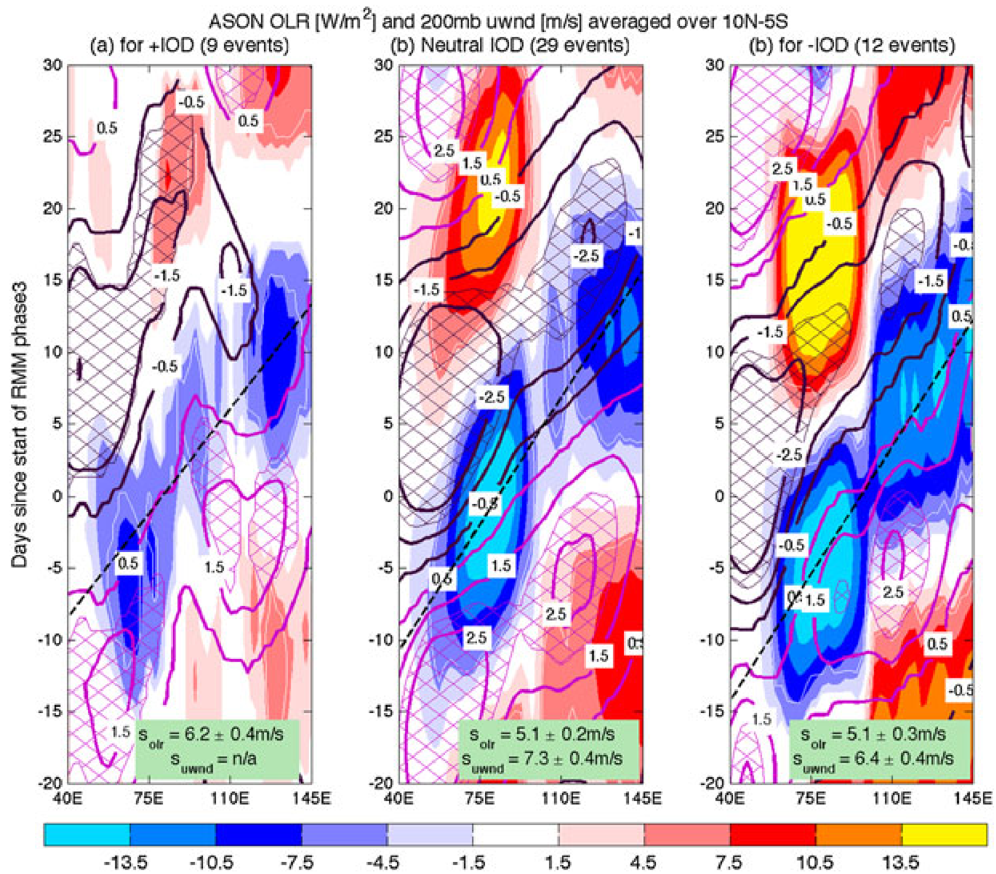

Figure 7. Time lagged composites of OLR (colored shading) and 200 mbar zonal wind anomalies (contours) for MJO events corresponding to Figure 6b. OLR and wind anomalies exceeding 95% level of confidence are enclosed by white contours and shaded with cross-hatches, respectively. Anomalies are averaged across 10°N and 5°S. Day 0 is when MJO events first enter RMM phase 3. S_{olr} and S_{uwnd} are the propagation speeds of the negative OLR anomalies and the trailing easterly wind anomalies, respectively. Speeds are obtained by fitting regression lines (shown for the OLR anomalies) through each anomaly distribution. The uncertainty in the speeds represents their 95% confidence interval.

is given by the 95% confidence interval as determined by a two-tailed Student's *t* test.

[32] A total of 29 MJO events were found to pass through RMM phase 3 during periods of neutral IOD. During this IOD mode, anomalous convection (negative OLR anomalies) associated with the MJO begins over the western Indian Ocean, intensifies over the eastern Indian Ocean, weakens over the Maritime Continent, but reinvigorates over the western Pacific (Figure 7b). Suppressed convective anomalies trail the enhanced convection in a similar fashion (not completely shown). The average propagation speed from 40°E to 145°E is ~5 m/s, as expected. Additionally, upper level westerly and easterly anomalies lead and trail convective activity, respectively. The easterly anomalies propagate through the region with an average speed of ~7 m/s, slightly faster than the convective anomalies. Altogether, Figure 7b seems like a very typical MJO event.

[33] MJO propagation during negative IOD follows a similar pattern but with a few subtle differences. A total of 12 MJO events were found to pass through RMM phase 3 during negative IOD. Fewer MJO events are expected since periods of negative IOD, by definition, are rarer than periods of neutral IOD. Over the Indian Ocean, convective activity is more concentrated to the east, where it appears slightly more intense than during neutral IOD (Figure 7c). Convective anomalies seem to strengthen in situ over the eastern Indian Ocean, from about lag –15 to –5 days and lag 7 to 17 days, before moving over to the Indonesian longitudes. This differs from the more continuous propagation during neutral IOD. Over the Maritime Continent, convective anomalies weaken but less so than during neutral IOD; the magnitude of the convective anomalies are consistent from 110°E to 145°E. In spite of these differences, the upper level easterlies and convective anomalies propagate at approximately the same speed as they do during neutral IOD.

[34] During positive IOD, MJO propagation takes on a strikingly different form (Figure 7a). A total of eight MJO events were found to pass through RMM phase 3 during positive IOD, fewer than during negative IOD. In general, MJO activity is much weaker than normal. Convective activity is relatively weak at all longitudes and does not peak over the eastern Indian Ocean, as it does during neutral and negative IOD. The suppressed or dry phase of the MJO is also relatively subdued over the Indian Ocean. The positive convective signal still manages to persist throughout the region at an average speed of ~6 m/s—slightly faster than the previous two cases. A breakdown in the MJO's wind field is also evident. Eastward propagation of the upper level easterly anomalies abruptly ends at around 90°E, after which they appear to propagate westward. Since there are two clear lines of propagation, the speed of the easterly anomalies cannot be determined by a single linear regression. This behavior is also observed, albeit to a lesser extent,

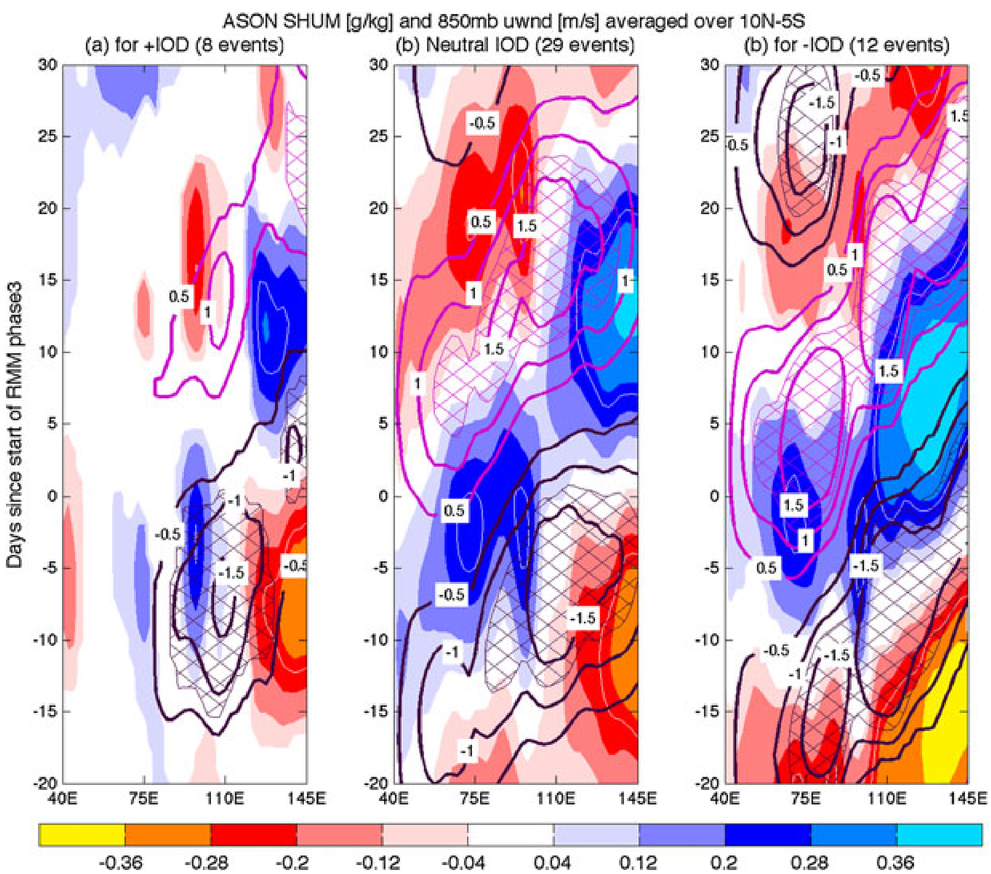

Figure 8. Like Figure 7 but with 850 mbar zonal winds (contours) and low-level specific humidity (grams/kilogram) averaged over 850 mbar to 500 mbar (shading).

in the leading westerly anomalies. However, these apparent westward propagating signals, while interesting, are not statistically significant.

[35] Figure 8 is similar to Figure 7, except that the contours now represent 850 mbar zonal winds and the shadings now represent specific humidity anomalies averaged from 850 mbar to 500 mbar. Once again, the wind anomalies appear strongest during negative and neutral IOD but weakest during positive IOD. During negative and neutral IOD, coherent 850 mbar wind anomalies are observed to propagate across the Indian Ocean (Figures 8b and 8c). During positive IOD, however, the 850 mbar wind anomalies do not extend west of 75°E, and the trailing low-level westerly anomalies are especially weak (Figure 8a). A similar relationship is seen in the low-level humidity anomalies. During neutral and negative IOD, positive and negative low-level moisture anomalies shadow the MJO's active and suppressed convective phases, respectively (Figures 7b and 7c). On the other hand, the low-level moisture anomalies associated with MJO events are weaker and less structured during positive IOD. Since sufficient low-level moisture is a necessary ingredient for convection, the absence of robust moisture anomalies seen in Figure 8a corresponds well to the weak convection seen in Figure 7a. This effect likely stems from the overall reduction in low-level moisture during positive IOD, shown in Figure 2.

[36] There is also noticeable asymmetry in the apparent effect of the IOD on MJO events. From Figures 6, 7, and 8, we observe that MJO events occurring during negative IOD are at best slightly stronger than MJO events occurring during neutral IOD. In contrast, MJO events that happen during positive IOD appear much weaker than those that occur during neutral IOD. This lopsided effect is likely due to the asymmetry in the IOD's forcing. From Figures 2 and 3, it is clear that the forcings associated with positive IOD is more substantial than those associated with negative IOD. This is also reflected in the skewness of the DMI. For the time period under study, ASON months from 1979 to 2010, the DMI has a positive skew of approximately 0.63. In other words, since positive IOD events were on average stronger and more frequent than negative IOD events, their composite effect had a much greater impact on the MJO.

3.4. Possible Mechanism for IOD-MJO Interaction

[37] Based on the IOD's forcings (Figures 2 and 3), one could reasonably surmise that the conditions associated with positive IOD are unfavorable for the MJO. That is, the reduced low-level humidity, higher surface pressure, and increased low-level divergence over the eastern Indian Ocean and the Maritime Continent are indicative of a more stable atmosphere, which would limit a development of a large-scale convective anomaly; this anomalously stable atmosphere is reinforced by the weakened zonal gradient of the SST over the Indian Ocean. Conversely, this line of thought would predict that the contrasting conditions associated with negative IOD will have a favorable effect on the MJO. While this rudimentary reasoning may be true to some extent, the complex behavior of the MJO requires a more subtle explanation. In the remainder of this section, previously suggested MJO theories are briefly reviewed, and an attempt is made to explain the relationship between the IOD and MJO in the context of those theories.

[38] Here we consider two schools of MJO theory. In one group, the MJO is considered as a variation of the equatorial moist Kelvin wave. The wave-CISK [e.g., *Lau*, 1987] and frictional wave-CISK [e.g., *Wang*, 1988; *Salby and Hendon*, 1994] are examples of theories in this group. In short, the wave-CISK theory predicts that the equatorial Kelvin wave becomes unstable when its convective heating interacts with low-level moisture convergence [*Lindzen*, 1974]. Without further modifications, however, these unstable wave-CISK Kelvin modes have phase speeds several times that of the MJO and maximum growth rates at the smallest scales [e.g., *Lau*, 1987]. As a result, wave-CISK theory has been modified to include a frictional boundary layer in the system [e.g., *Wang*, 1988]. In the frictional wave-CISK theory, instability arises through friction-induced (rather than wave-induced) moisture convergence within the boundary layer. Frictional wave-CISK also introduces an unstable coupled Kelvin-Rossby mode [e.g., *Wang and Rui*, 1990; *Salby and Hendon*, 1994]. This coupling leads to slower propagation speeds (about 5 m/s) and favors the expansion of planetary-scale disturbances [*Wang and Rui*, 1990]. The existence of the slow, planetary-scale moist Kelvin-Rossby mode depends on the low-tropospheric moisture amount, which is a function of SST. In *Wang and Rui* [1990], the phase speed of the Kelvin-Rossby mode becomes faster as SST, and low-tropospheric moisture contents becomes lower. This suggests that in their theory, MJO prefers a moister atmosphere.

[39] In another group, the MJO is viewed as a "moisture mode" [e.g., *Raymond*, 2001; *Sugiyama*, 2009a, b; *Sobel et al.*, 2001; *Sobel and Maloney*, 2012, 2013], where the accumulation of the tropospheric moisture is crucial for the development of the MJO convection [*Blade and Hartmann*, 1993]. The theories that fall into this group emphasize thermodynamic feedbacks, such as cloud-radiation interaction [*Raymond*, 2001], rather than the interaction between convection and wave-induced circulation. The seasonal mean forcing associated with the positive IOD would be an unfavorable condition for the development of the MJO with respect to this theory. That is, the stable atmosphere over the eastern Indian Ocean, associated with the reduced zonal SST gradient over the Indian Ocean, would inhibit the accumulation of the low-level humidity, thereby weakening the MJO in that region. With this in mind, the variations in lower troposphere humidity between IOD events, as shown in Figure 2, might explain why MJO events appear stronger during negative IOD than during positive IOD.

4. Summary and Conclusion

[40] Our results show that the MJO is affected by the large-scale atmospheric variations associated with the IOD. The eastern Indian Ocean and Maritime Continent regions appear less favorable for MJO development during positive IOD than during weak or negative IOD. Evidence of this is given by the slightly stronger than normal MJO propagation through the region during negative IOD and the relatively weak propagation during positive IOD (Figures 6, 7, and 8). This result is not entirely surprising given that previous studies, namely *Shinoda and Han* [2005] and *Kug et al.* [2009], showed that subseasonal variability over the Indian Ocean is reduced during positive IOD; *Kug et al.* [2009] showed

that this was true for 2–70 day low-level zonal wind variability, while *Shinoda and Han* [2005] proved this result for 6–30 day OLR variability.

[41] One likely explanation for these relationships is that the SST gradient and the low-level wind anomalies associated with positive IOD inhibits low-level convergence over the eastern Indian Ocean and as result suppresses MJO development in that region. This postulation is supported by MJO theories, such as wave-CISK, frictional wave-CISK, and MJO moisture mode theories, which describe the proliferation of MJO-like disturbances as being critically dependent on sufficient low-level moisture accumulation. *Shinoda and Han* [2005] came to a similar conclusion when explaining the reduction of 6–30 day OLR variability during positive IOD. They showed that moisture convergence ($\nabla \cdot (q\mathbf{U})$) over the southeastern tropical Indian Ocean is strongly correlated (0.82) with 6–30 day OLR variability in that region. They also found that moisture convergence over the southeastern tropical Indian Ocean is better correlated with the DMI (0.85) than with local SST (0.66) [*Shinoda and Han*, 2005]. The latter result underscores the importance of the zonal SST gradient in maintaining moisture convergence in the eastern Indian Ocean.

[42] It is also quite possible that other factors could affect MJO development during IOD events. For example, *Kug et al.* [2009] argues that during positive IOD an anomalous westerly vertical wind shear over the Indian Ocean inhibits eastward propagation of the MJO through this region. It would be a worthwhile endeavor to explore the importance of these other effects on MJO development. Still, while these unknown factors may be important, the supply and distribution of low-level moisture will always be a major contributing factor to MJO development and propagation.

[43] The combined effects of the IOD and ENSO on MJO propagation also warrants further investigation. Even though the IOD has the capacity to independently modulate intraseasonal variability over the Indian Ocean, ENSO can make its own significant contribution. A logical extension of this study would be to broaden the regional scope to include the equatorial Pacific and analyze how different IOD/ENSO configurations affect MJO propagation throughout the entire region.

[44] **Acknowledgments.** Thanks to Adam Sobel for providing insightful comments during the preliminary stages of this work. We would also like to thank our two anonymous reviewers for their thorough assessment of this paper. Earle Wilson and Arnold Gordon were supported by the Office of Naval Research under Grant N00014-10-1-0317 to the Lamont-Doherty Earth Observatory of Columbia University. Daehyun Kim acknowledges the support of the National Aeronautics and Space Administration under Grant NNX09AK34G. This research was also funded in part under the Cooperative Institute for Climate Applications Research (CICAR) award number NA08OAR4320754 from the National Oceanic and Atmospheric Administration, U.S. Department of Commerce. The statements, findings, conclusions, and recommendations are those of the author(s) and do not necessarily reflect the views of the National Oceanic and Atmospheric Administration or the Department of Commerce. Lamont-Doherty Earth Observatory contribution number 7661.

References

Bladé, I., and D. L. Hartmann (1993), Tropical intraseasonal oscillations in a simple nonlinear model, *J. Atmos. Sci*, *50*(17), 2922–2939.

Duchon, C. (1979), Lanczos filtering in one and two dimensions, *J. Appl. Meteorol*, *18*, 1016–1022.

Hendon, H. H., M. C. Wheeler, and C. Zhang (2007), Seasonal dependence of the MJO-ENSO relationship, *J. Climate*, *20*, 531–543, doi:10.1175/JCLI4003.1.

Kalnay, E., et al. (1996), The NCEP/NCAR 40-year reanalysis project , *Bull. Amer. Meteor. Soc.*, *77*, 437–471.

Kessler, W. S., M. J. McPhaden, and K. M. Weikmann (1995), Forcing of Kelvin waves in the equatorial Pacific, *J. Geophys Res.*, *10*, 613–10,631.

Knutson, R. R., and K. M. Weickmann (1987), 30–60 day atmospheric oscillations: Composite life cycles of convection and circulation anomalies, *115*, 1407–1436.

Kug, J. S., K. P. Sooraj, F. F. Jin, J. J. Lou, and M. Kwon (2009), Impact of Indian Ocean Dipole on high-frequency variability over the Indian Ocean, *Atmospheric Research*, *94*, 134–139, doi:10.1016/j.atmosres.2008.10.022.

Lau, K. M. (1987), Origin of low-frequency (intraseasonal) oscillations in the tropical atmosphere. Part I: Basic theory, *J. Atmos. Sci.*, *44*, 950–972.

Liebmann, B., and C. A. Smith (1996), Description of a complete (interpolated) outgoing longwave radiation dataset, *Bull. Amer. Meteor. Soc.*, *77*, 1275–1277.

Lindzen, R. S. (1974), Wave-CISK in the tropics, *J. Atmos. Sci.*, *31*, 156–179.

Madden, R. A., and P. R. Julian (1971), Detection of a 40–50 day oscillation in the zonal wind in the tropical Pacific, *J. Atmos. Sci*, *28*, 702–708.

Madden, R. A., and P. R. Julian (1972), Description of global scale circulation cells in the Tropics with a 40–50 day period, *J. Atmos. Sci*, *29*, 1109–1123.

Matthews, A. J. (2008), Primary and successive events in the Madden-Julian oscillation, *Q. J. R. Meteorolog. Soc.*, *134*, 439–453.

Panofsky, H. A., and G. W. Brier (1958), *Some Applications of Statistics to Meteorology*, 114–116, The Pennsylvania State University, Philadelphia.

Raymond, D. J. (2001), A new model of the Madden-Julian Oscillation, *J. Atmos. Sci.*, *58*, 2807–2819, doi:10.1175/1520-0469(2001)058<2807:ANMOTM>2.0.CO;2.

Roundy, P. E., C. J. Schreck, and J. M. A. (2009), Contributions of convectively coupled equatorial Rossby waves and Kelvin waves to the Real-Time Multivariate MJO indices, *Mon. Weather Rev.*, *137*, 469–478, doi:10.1175/2008MWR2595.1.

Saji, N. H., and T. Yamagata (2003), Structure of SST and surface wind variability during Indian Ocean Dipole mode years: COADS observations, *J. Climate*, *16*, 2735–2751, doi:10.1175/1520-0442(2003)016<2735:SOSASW>2.0.CO;2.

Saji, N. H., P. N. Vinayachandran, and T. Yamagata (1999), A dipole mode in the tropical Indian Ocean, *Nature*, *401*, 360–363.

Salby, M. L., and H. H. Hendon (1994), Intraseasonal behavior of clouds, temperature and motion in the Tropics, *J. Atmos. Sci*, *51*, 2207–2224.

Shinoda, T., and W. Han (2005), Influence of the Indian Ocean Dipole on atmospheric subseasonal variability, *J. Climate*, *18*, 3891–3909, doi:10.1175/JCLI3510.1.

Smith, T., R. Reynolds, T. C. Peterson, and J. Lawrimore (2008), Improvements to NOAA's historical merged land-ocean surface temperature analysis (1880-2006), *J. Climate*, *21*, 2283–2296, doi:10.1175/2007JCLI2100.1.

Sobel, A., J. Nilsson, and L. M. Polvani (2001), The weak temperature gradient approximation and balanced tropical moisture waves., *J. Atmos. Sci.*, *58*, 3650–3665.

Sobel, A., and E. Maloney (2012), An idealized semi-empirical framework for modeling the Madden–Julian oscillation, *J. Atmos. Sci.*, *69*, 1691–1705, doi:10.1175/JAS-D-11-0118.1.

Sobel, A., and E. Maloney (2013), Moisture modes and the eastward propagation of the MJO, *J. Atmos. Sci.*, *70*, 187–192, doi:10.1175/JAS-D-12-0189.1.

Sooraj, K. P., D. Kim, J. S. Kug, S. W. Yeh, F. F. Jin, and I. S. Kang (2009), Effects of low-frequency zonal wind variation on high frequency atmospheric variability over the tropics, *Clim. Dyn.*, *33*, 495–507, doi:10.1007/s00382-008-0483-6.

Straub, K. (2012), MJO initiation in the Realtime Multivariate MJO index, *J. Climate*, *26*, 1130–1151, doi: 10.1175/JCLI-D-12-00074.1.

Sugiyama, M. (2009a), The moisture mode in the quasi-equilibrium tropical circulation model. Part I: Analysis based on the weak temperature gradient approximation, *J. Atmos. Sci.*, *66*, 1507–1523, doi:10.1175/2008JAS2690.1.

Sugiyama, M. (2009b), The moisture mode in the quasi-equilibrium tropical circulation model. Part II: Nonlinear behavior on an equatorial beta plane, *J. Atmos. Sci.*, *66*, 1525–1542, doi:10.1175/2008JAS2691.1.

Wang, B. (1988), Dynamics of tropical low-frequency waves: An analysis of the moist Kelvin wave, *J. Atmos. Sci.*, *45*, 2051–2065.

Wang, B., and H. Rui (1990), Dynamics of the coupled moist Kelvin-Rossby wave on an equatorial beta-plane, *J. Atmos. Sci.*, *47* (4), 397–413.

Webster, P. J., A. M. Moore, J. P. Loschnigg, and R. R. Leben (1999), Coupled ocean-atmosphere dynamics in the Indian Ocean during 1997–98, *Nature*, *401*, 356–359.

Wheeler, M. C., and M. N. Kiladis (1999), Convectively coupled equatorial waves: Analysis of clouds and temperature in the wavenumber-frequency domain, *J. Atmos. Sci.*, *56*, 374–399.

Wheeler, M. C., and H. H. Hendon (2004), An all-season real-time multivariate MJO index: Development for an index for monitoring and prediction, *Mon. Weather Rev.*, *132*, 1917–1932.

Zhang, C. (2005), Madden Julian Oscillation, *Reviews of Geophysics*, *43,* RG2003, doi:10.1029/2004RG000158.

Zhang, C., and J. Gottschalk (2002), SST anomalies of ENSO and the Madden-Julian oscillation in the equatorial Pacific, *J. Climate*, *15*, 2429–2445.